



# Fitness-for-Service Analysis of Reactor Components under Flexible Load- Following Operating Conditions

July 2024

*Changing the World's Energy Future*

Minh Tran, Ondrej Muransky, Benjamin W Spencer



**DISCLAIMER**

This information was prepared as an account of work sponsored by an agency of the U.S. Government. Neither the U.S. Government nor any agency thereof, nor any of their employees, makes any warranty, expressed or implied, or assumes any legal liability or responsibility for the accuracy, completeness, or usefulness, of any information, apparatus, product, or process disclosed, or represents that its use would not infringe privately owned rights. References herein to any specific commercial product, process, or service by trade name, trade mark, manufacturer, or otherwise, does not necessarily constitute or imply its endorsement, recommendation, or favoring by the U.S. Government or any agency thereof. The views and opinions of authors expressed herein do not necessarily state or reflect those of the U.S. Government or any agency thereof.

# **Fitness-for-Service Analysis of Reactor Components under Flexible Load-Following Operating Conditions**

**Minh Tran, Ondrej Muransky, Benjamin W Spencer**

**July 2024**

**Idaho National Laboratory  
Idaho Falls, Idaho 83415**

**<http://www.inl.gov>**

**Prepared for the  
U.S. Department of Energy  
Under DOE Idaho Operations Office  
Contract DE-AC07-05ID14517**

# FITNESS-FOR-SERVICE ANALYSIS OF A LIGHT WATER REACTOR PRESSURE VESSEL UNDER COMPLEX OPERATING CONDITIONS

Minh N. Tran<sup>1,2</sup>, Ondrej Muransky<sup>1,2</sup>, and Benjamin W. Spencer<sup>3</sup>

<sup>1</sup>Australian Nuclear Science and Technology Organisation, Lucas Heights, Sydney, NSW, Australia

<sup>2</sup>University of New South Wales, Sydney, NSW, Australia

<sup>3</sup>Idaho National Laboratory, Idaho Falls, ID, United States of America

## ABSTRACT

*Conventional power-generation plants, including nuclear plants, have been traditionally designed to provide a steady baseload energy capacity, optimizing output efficiency while minimizing variable costs. However, the growing adoption of large-scale renewable energy-generation systems, which rely on intermittent sources such as solar and wind, has introduced more variability into the energy supply in interconnected electricity grids. As a result, the next generation of power plants needs to operate in what is known as load-following mode, requiring flexible adjustments in electricity production to align with the energy demand on the grid. This transition from the steady baseload operation to load-following operating conditions can significantly increase the number of times various plant components are exposed to transient stresses. This increased thermomechanical cycling can lead to accelerated material degradation, thereby elevating the risk of premature component failure. It becomes imperative to conduct a comprehensive analysis of fatigue, creep-fatigue, and stress corrosion cracking life to assess the resilience of the various engineering components under these flexible load-following operating conditions.*

*This study aims to develop a comprehensive numerical model of a light-water reactor pressure vessel (RPV) to investigate its degradation under various operating scenarios. This coupled thermomechanical finite element analysis evaluated the stress response of the RPV caused by considering fluctuations in thermal and mechanical loads caused by the varying pressure and temperature occurring during the load-following operation. Critical locations on the RPV are subsequently identified based on the stress response. The stress intensity factors for the postulated flaws at those locations are then calculated, followed by an evaluation of the reactor's life in accordance with the American Society of Mechanical Engineers Boiler and Pressure Vessel Code Section XI. This comprehensive life assessment covers a number of transients expected during*

*the flexible load-following operation, providing invaluable insights into the RPV's structural integrity. Moreover, the development methodology can be adapted to other reactor components, as well as components of conventional power stations affected by varying operating conditions.*

Keywords: Reactor Pressure Vessel, Fitness-for-Service, Finite Element Analysis, Fatigue Crack Growth, Stress Intensity Factor, Linear Elastic Fracture Mechanics

## 1. INTRODUCTION

Conventional power plants, including nuclear plants, have traditionally been designed to serve as steady baseload electricity sources. However, with the growing adoption of renewables, these traditional baseload electricity providers are expected to operate in load-following operation mode [1-3]. Operating in a flexible load-following mode, these power plants face the challenge of subjecting their pressure vessels and pressure boundary components to additional thermomechanical cycles [4, 5]. This, in turn, can accelerate the degradation of employed materials, elevating the risk of premature failure of various components. Therefore, it is essential to perform new fitness-for-service assessments that account for additional thermomechanical cycling stemming from the load-following operation. Moreover, since there are plans to extend the original 40 year design life of current nuclear power plants to 80 years [6], ageing-related material issues can introduce further complexities to structural integrity.

This study aims to develop a comprehensive numerical model of a light-water reactor pressure vessel (RPV) for assessing the structural integrity of nuclear power plant components under complex operating conditions. A Westinghouse-type two-loop pressurized-water reactor is utilized as a case study due to the availability of pertinent data [7]. This paper describes a coupled thermomechanical stress analysis of the Westinghouse-type RPV and its associated nozzles, considering typical normal service transients, including

load-following mode, is conducted. Critical locations on the RPV are identified based on the stress response. The stress intensity factors (SIFs) for the postulated flaws are then calculated in these critical locations, followed by an evaluation of the reactor's fatigue life in a light-water reactor environment following the American Society of Mechanical Engineers (ASME) Boiler and Pressure Vessel Code Section XI.

## 2. METHODOLOGY

This section summarizes the three-dimensional (3D) finite element (FE) model developed for the thermomechanical stress analysis. The internal pressure and end-cap loads are applied as mechanical loads, while the thermal loads take the form of heat transfer coefficients. The SIFs are computed according to the ASME Code Section XI Article A-3000, and the fatigue crack growth (FCG) is performed as specified in the ASME Code Section XI Article A-4000.

### 2.1 Finite Element Model and Materials

A solid FE model of the Westinghouse-type reactor (AP1000) was developed based on the dimensions outlined in the design control documents. These documents are openly accessible within the U.S. Nuclear Regulatory Commission ADAMS public repository [7]. Figure 1 shows the 3D solid model of the RPV, accompanied by a quarter cross-section to provide the inside view of the RPV—the model was developed in the open-source FreeCAD software package [8]. The model consists of the RPV shells and heads, four inlet nozzles, two outlet nozzles, and two injection nozzles.

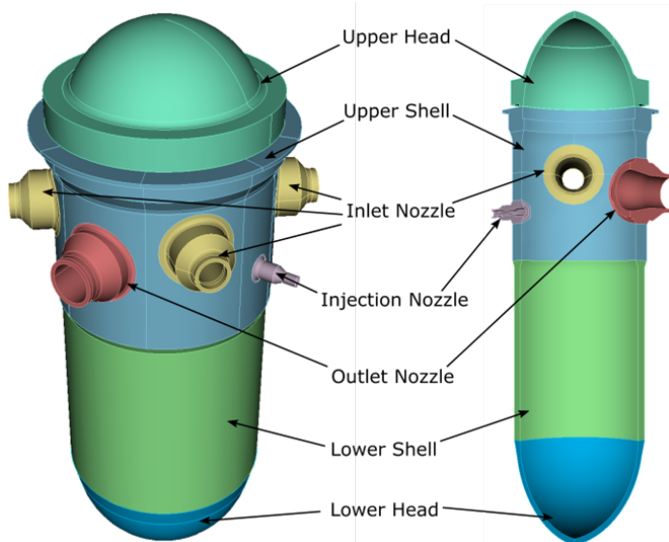


**FIGURE 1:** MODEL OF RPV, INLET, OUTLET, AND INJECTION NOZZLES

The developed solid model was meshed using the Coreform Cubit meshing software [9], which allows for meshing of the complex RPV geometry. Figure 2 (a) provides a 3D quarter-symmetry meshed FE model of the full RPV containing 242,837 8-node linear hexahedral elements. Since the quarter-symmetry model was used for the thermomechanical analysis, symmetric

boundary conditions were applied on surfaces as shown in Figure 2 (a). Lastly, a node located at the base of the FE model is effectively constrained against displacement in the axial direction.

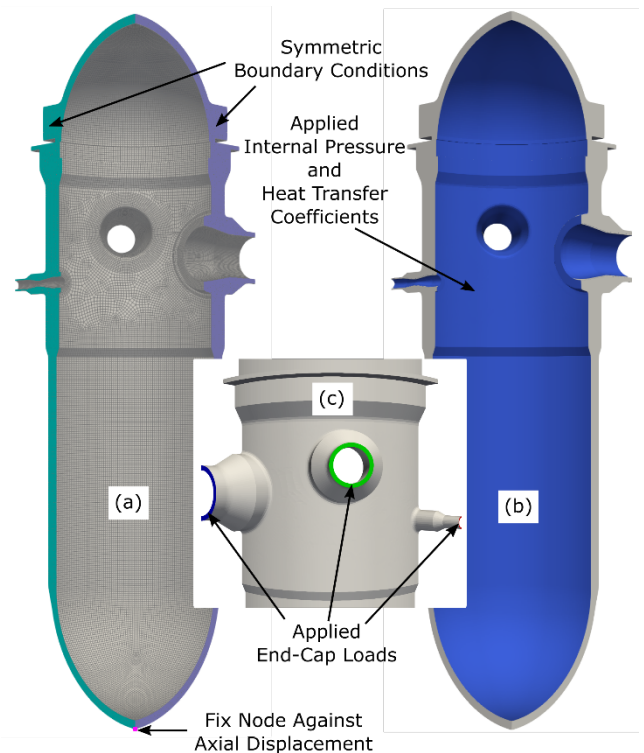


**FIGURE 2:** (A) FE MESH OF A QUARTER-SYMMETRY 3-D RPV SHOWING BCS, (B) APPLIED INTERNAL PRESSURE AND HEAT TRANSFER COEFFICIENTS, AND (C) APPLIED END-CAP LOADS

The modelling of the structural integrity of reactor components involves solving coupled systems of partial differential equations. The thermomechanical stress analysis was conducted using BlackBear [10], which leverages the capabilities of the MOOSE framework (Multiphysics Object-Oriented Simulation Environment) [11], to solve these coupled partial differential equations. For simplicity, the RPV and its nozzles are assumed to be composed entirely of SA-508 steel. The temperature-dependent properties for SA-508 steel used in the analysis are referenced from [12].

### 2.2 Applied Loads

To provide a fitness-for-service evaluation for components within the reactor system, the RPV, designed and constructed to the requirements for Class 1 components in the ASME Code Section III, generally undergoes assessment spanning design, service, and test conditions. In this study, the fitness-for-service evaluation for the RPV only considers the design conditions as a representative example of the process. Within this scope, the analysis focuses on pressure and temperature loadings selected as the basis for the design, expected to occur during normal operating conditions. Evaluating the normal conditions, referred

to as Level A Service Conditions, typically includes an assessment of fatigue resulting from cyclic stresses. These stresses arise during system startup, operation in the design power range, hot standby, and system shutdown.

Transient	Description	Cycles
1	Reactor coolant pump startup and shutdown (cycles of start and stop)	
1a	Cold startup transients	200
1b	RCS heat-up, cool-down	200
1c	Hot functional RCP stops, starts	400
1d	Transients and miscellaneous	2200
2a	Heat-up at 100°F/hr	200
2b	Cool-down at 100°F/hr	200
3a	Unit loading between 0% and 15% full power (FP)	500
3b	Unit unloading between 15% and 0% FP	500
4a	Unit loading at 5%/min between 15% and 100% FP	2000
4b	Unit unloading at 5%/min between 100% and 15% FP	2000
5a	Step load increase of 10% FP between 15% and 100% FP	3000
5b	Step load decrease of 10% FP between 100% and 15% FP	3000
6	Large step load decrease with steam dump	200
7	Steady-state fluctuation and load regulation	
7ai	Initial	75000
7aia	Initial	75000
7bi	Random	2300000
7bii	Random	2300000
7c	Load regulation within 15% to 95% FP	750000
8	Boron concentration equalization	2900
9	Feedwater cycling at hot shutdown	
9a	Mode 1 (every 2 hrs)	3000
9b	Mode 2 (every 24 mins)	15000
10	Core lifetime extension	40
11	Feedwater heaters out of service	180
12	Refueling	40
13	Turbine roll test	20
14	Primary-side leakage test	200
15	Secondary-side leakage test	80
16	Core makeup tank high-pressure injection test	5
17	Passive residual heat removal tests	5
18	Reactor coolant system makeup	2820
19	Daily load following operation	17800

**TABLE 1:** SERVICE LEVEL A DESIGN TRANSIENTS, DESCRIPTIONS, AND NUMBER OF CYCLES EXPECTED DURING NORMAL FLEXIBLE LOAD-FOLLOWING OPERATING CONDITION

Table 1 presents an overview of the design transients, along with corresponding descriptions, and the number of events, which are necessary for evaluating fatigue life under Level A Service Conditions [7]. These design transients, along with corresponding descriptions, were used to derive the applied internal pressure, end-cap loads, and heat transfer coefficients for the RPV, inlet, outlet, and injection nozzles. The end-cap loads are calculated from the internal pressure by the simple formula given below:

$$P_{\text{endcap}} = \frac{P_{\text{int}} ID^2}{OD^2 - ID^2} \quad (1)$$

where  $P_{\text{endcap}}$  is the end-cap pressure,  $P_{\text{int}}$  is the internal pressure,  $ID$  is the inner diameter, and  $OD$  is the outer diameter.

The application of internal pressure to the interior surfaces of the RPV and its nozzles is depicted in Figure 2 (b). The induced end-cap loads in Equation (1) were applied to the free-end of the nozzles in the form of tensile axial pressures as illustrated in Figure 2 (c).

The heat transfer coefficient (or film coefficient) is a quantitative characteristic of convective heat transfer between a fluid (water) and the wall surface (inner surface of the RPV and its nozzles). There are two modes of convective heat transfer: natural (or free) convection and forced convection. Natural convection involves heat transfer driven solely by the fluid's inherent motion. In forced convection, external forces actively influence the fluid's movement. Throughout reactor system operation, forced convection is the dominant mode of heat transfer, stemming from external forces, such as coolant pumps, propelling the fluid's movement. When the reactor system is not active, natural convection takes precedence, in the absence of external forces, allowing fluid motion to be guided purely by natural influences.

For natural convection in enclosed spaces, the internal heat transfer coefficients can be calculated with [13]:

$$Nu_f = 0.55 (Gr_f Pr_f)^{1/4}$$

$$\frac{hd_e}{k} = 0.55 \left[ \left( \frac{g\beta\Delta T d_e^3}{\nu^2} \right) Pr_f \right]^{1/4} \quad (2)$$

where  $Nu_f$  is the Nusselt number,  $Gr_f$  is the Grashof number,  $Pr_f$  is the Prandtl number,  $h$  is the heat transfer coefficient,  $d_e$  is the equivalent diameter,  $k$  is the thermal conductivity,  $g$  is the acceleration of gravity,  $\beta$  is the temperature coefficient of volume expansion,  $\Delta T$  is the temperature difference between water and inner surface (assumed to be 3°C), and  $\nu$  is the kinematic viscosity.

For forced convection, when considering fully developed turbulent flow within smooth tubes for fluid heating, the corresponding internal heat transfer coefficients are given by [13]:

$$Nu_d = 0.023 Re_d^{0.8} Pr^{0.4}$$

$$\frac{hd_e}{k} = 0.023 \left( \frac{Gd_e}{\mu} \right)^{0.8} Pr^{0.4} \quad (3)$$

where  $Nu_d$  is the Nusselt number,  $Re_d$  is the Reynolds number,  $Pr$  is the Prandtl number,  $h$  is the heat transfer coefficient,  $d_e$  is the equivalent diameter,  $k$  is the thermal conductivity,  $\mu$  is the dynamic viscosity, and  $G$  is the mass velocity.

The thermophysical properties of water, as functions of pressure and temperature, are readily accessible in [13-15], providing necessary parameters for Equations (2) and (3). The heat transfer coefficient,  $h$ , in Equations (2) and (3) can

subsequently be calculated for natural and forced convections, respectively. These heat transfer coefficients are then applied to the interior surfaces of the RPV and its nozzles as shown in Figure 2 (b). Since reactor systems are typically well-insulated, a reasonable assumption is that no heat loss occurs across the exterior surfaces. Furthermore, the heat-up and cool-down rates were maintained below 55°C/hour (55 K/hour) for temperature above 175°C (450 K) within the reactor system. The material's stress-free temperature was set at an ambient temperature of 21°C (294 K).

### 2.3 Stress Intensity Factor

After computing the stress field for the full RPV through the FE model, the subsequent stage focused on determining the SIFs, employing the weight function methodology. Guidance for calculating SIFs utilizing the weight function method is outlined in the ASME Section XI, Nonmandatory Appendix A, Article A-3000 [16]. The weight function approach enables calculating SIFs for arbitrary stress distributions acting normal to the crack plane when addressing surface-breaking flaws. The weight function approach relies on the superposition principle, which was originally proposed by Bueckner [17] and subsequently elaborated on by Rice [18]. The superposition principle demonstrates that the SIF on a crack face stemming from a load state, achieved through applied far-field surface tractions, is equivalent to the SIF arising from the application of tractions at the location of the crack due to the same load state if that crack was not present.

In this study, 2D semielliptical surface-breaking flaws in both axial and circumferential directions were postulated on the interior of the RPV at the location where the resulting stress fields from the applied cyclic loadings were the most severe. The SIFs due to mode I fracture,  $K_I$ , were calculated by integrating the product of the weight function,  $m(x, a)$ , given in the ASME Code Section XI Article A-3000 [16] and the stress distribution,  $\sigma(x)$ , along the crack plane from the FE model given as:

$$K_I(a) = \int_0^a m(x, a) \sigma(x) dx \quad (4)$$

where  $x$  is the through-wall distance from the inner surface moving positive toward the tip of the crack and  $a$  is the crack depth. The initial crack depth,  $a_0$ , was assumed to be 25% of the wall thickness,  $t$ . The initial half crack length,  $c_0$ , was assumed to be 3 times the initial crack depth, which is in accordance with the ASME Code Section XI Appendix L [16]. The flaw aspect ratio,  $a/c$ , was allowed to vary throughout calculation of the SIFs as the crack evolved.

The fracture toughness of a material hinges on two key attributes  $K_{Ia}$  and  $K_{Ic}$  (MPa√m), which represent critical values of the SIF. The  $K_{Ia}$  value is based on the lower bound of crack arrest critical  $K_I$  values, whereas the  $K_{Ic}$  value is based on the lower bound of static initiation critical  $K_{Ic}$  values, both of which are functions of temperature. For crack progression to ensue, the SIFs must remain within the bounds of  $K_{Ia}$  and  $K_{Ic}$ . The values

for  $K_{Ia}$  and  $K_{Ic}$  are sourced from ASME Code Section XI Article A-4200 [16] given as:

$$K_{Ic} = 36.5 + 22.783 \exp[0.036 (T - RT_{NDT})] \quad (5a)$$

$$K_{Ia} = 29.4 + 13.675 \exp[0.0261 (T - RT_{NDT})] \quad (5b)$$

where  $T$  is the temperature (°C) and  $RT_{NDT}$  is the reference nil-ductility temperature (°C).

### 2.4 Fatigue Crack Growth

For a given material, the crack growth behavior can be correlated by the relationship between the cyclic crack growth rate,  $da/dN$ , and the SIF range,  $\Delta K_I = K_{max} - K_{min}$ . The FCG rate for a material can be divided into three regimes: low growth rates, mid-range growth rates, and high growth rates. Test data and corresponding fitted curves are generally presented on a log-log plot. At mid-range growth rates, the fitted curve often forms a straight line. This linear relationship can be described by the Paris equation [19]:

$$\frac{da}{dN} = C(\Delta K_I)^n \quad (6)$$

where  $C$  is the scaling constant and  $n$  is the slope of the log ( $da/dN$ ) versus log ( $\Delta K_I$ ).

Fatigue cycles characterized by a higher stress ratio,  $R = K_{min}/K_{max}$ , exhibit an accelerated rate of crack growth, whereas cycles in which  $\Delta K_I$  falls below the threshold  $\Delta K_{th}$ , the FCG rate becomes negligible. The values for  $\Delta K_{th}$  are sourced from ASME Code Section XI Article A-4300 [16] given as:

$$\Delta K_{th} = 5.5 \text{ for } R < 0 \quad (7a)$$

$$\Delta K_{th} = 5.5 (1 - 0.8R) \text{ for } 0 \leq R < 1.0 \quad (7b)$$

Particular to the SA-508 ferritic steel material exposed to light-water reactor environment, the FCG rate is provided in the ASME Code Section XI Article A-4000 [16].

In this study, the fatigue life, under thermo-mechanical cyclic loading, is evaluated through the application of linear elastic fracture mechanics (LEFM). The evaluation begins with the computation of  $K_{max}$  and  $K_{min}$  for each transient. Then, the SIF values,  $K_I$ , are determined whether they fall below the critical crack arrest value,  $K_{Ia}$ , at which the crack ceases to propagate and the analysis is terminated with no further crack growth. Conversely, if  $K_I$  reaches the fracture toughness value,  $K_{Ic}$ , at which unstable crack growth occurs, leading to failure, and the analysis is terminated. For SIF values falling between  $K_{Ia}$  and  $K_{Ic}$  ( $K_{Ia} \leq K_I \leq K_{Ic}$ ), the crack exhibits stable growth. Utilizing the superposition principle, the effects arising from cyclic loading attributed to each normal operating event,  $e$ , are aggregated across all transients,  $M$ , for a specified number of cycles from each transient per time period,  $\Delta N_e$ . The cumulative crack increment for a time period,  $\Delta a$ , is then determined as the sum of crack growth from each transient  $\Delta a_e$ . The final crack size is the sum of the initial crack and the total crack increment

for every time period. A flowchart of this procedure is outlined in Figure 3.

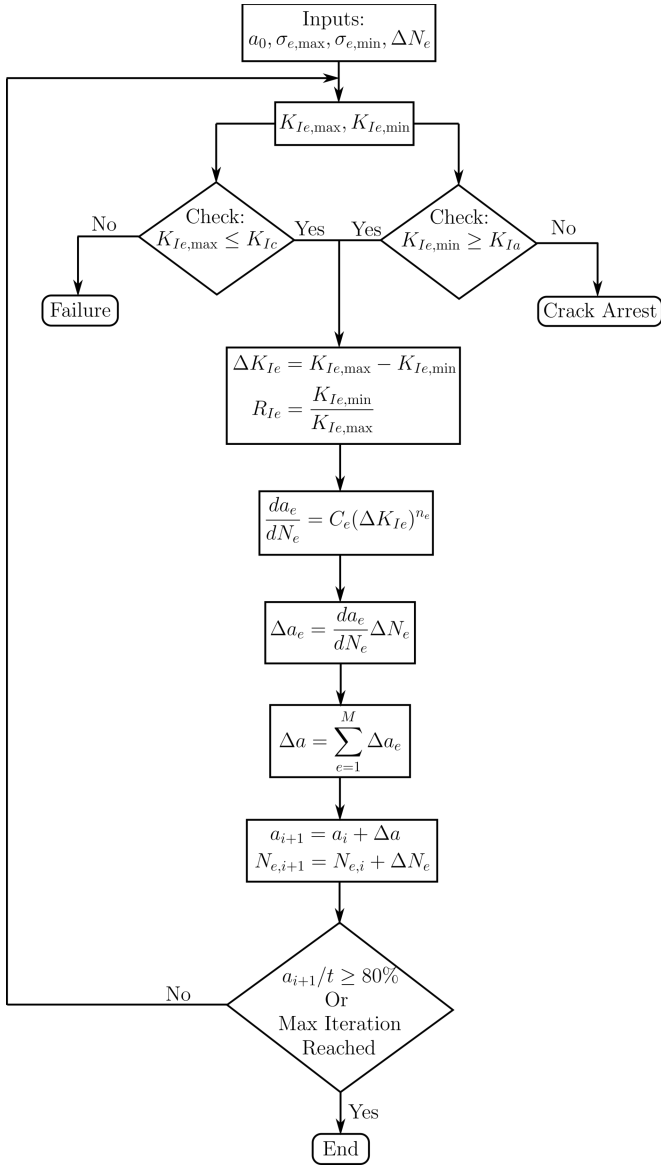


**FIGURE 3: FLOWCHART OF FATIGUE CRACK GROWTH HISTORY CALCULATION**

### 3. RESULTS AND DISCUSSION

This section provides an overview of the thermomechanical stress analysis outcomes and presents an evaluation of the fatigue life assessment of the RPV based on Westinghouse’s AP100 design, while considering a large number of events (transients), that are expected to occur during the flexible load-following operating condition of the reactor. This study performs fitness-for-service analysis considering 19 transients, summarized in Table 1.

#### 3.1 Thermomechanical Stress Results

The thermomechanical stress analysis of the RPV reveals that the two critical locations are situated in the injection nozzle region and the inlet nozzle region. Specifically, the injection nozzles are only active during two specific instances: Transient 12 (refueling process) for 40 cycles and Transient 16 (high-pressure injection test) for 5 cycles within the 60-year operational plant design objective. On the other hand, the inlet nozzles operate throughout almost all transients during normal operation. Consequently, a high-stress location in the inlet nozzle region, as depicted in Figure 4, was identified as the most critical from the fitness-for-service perspective.

Elevated stress levels around the inlet nozzle region become apparent during the cool-down period Transient 2b. The axial and hoop stress fields, with respect to the RPV shell, at the peak instance are presented in Figure 4 (a) and (b), respectively. As shown in Figure 4 (c), a section of the upper shell is highlighted, indicating the position of the peak hoop stress encountered in Transient 2b. Figure 4 (d) outlines the shortest path emanating from this critical location and cutting across the thickness. This path serves as the critical path for extracting stress profiles for a fatigue life analysis across all transients.

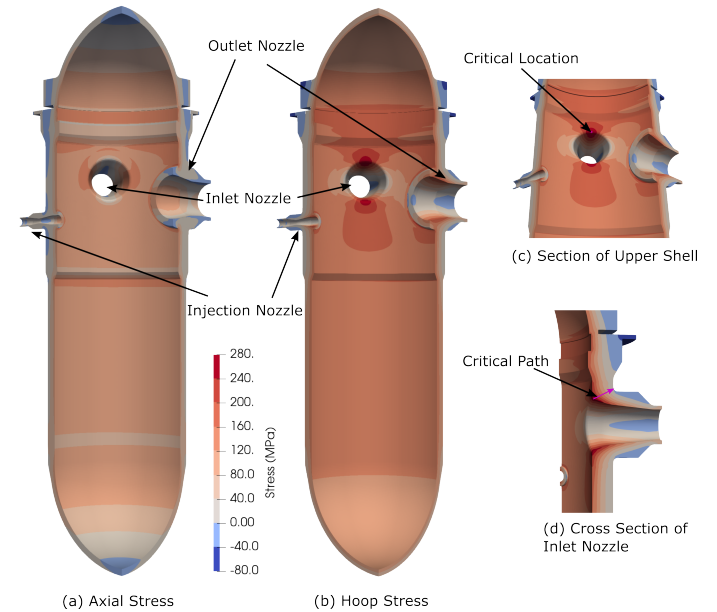


**FIGURE 4: (A) AXIAL AND (B) HOOP STRESS FIELDS, WITH RESPECT TO THE RPV SHELL, FOR COOL-DOWN TRANSIENT 2B, (C) SECTION OF THE UPPER SHELL SHOWING THE CRITICAL LOCATION, AND (D) CROSS SECTION OF THE INLET NOZZLE SHOWING THE CRITICAL PATH**

Figure 5 (a) depicts the maximum and minimum stress profiles during Transient 2 (heat-up and cool-down) along the above-defined critical path. The corresponding SIFs are then presented in Figure 5 (b). The figure reveals that the SIFs associated with the minimum stress profile remain almost constant. This means that these SIFs fall below the critical crack arrest threshold,  $K_{Ia}$ , shown in Equation (5b). The difference

between the maximum and minimum SIFs defines the SIF ranges  $\Delta K_I$  as illustrated in Figure 5 (b).

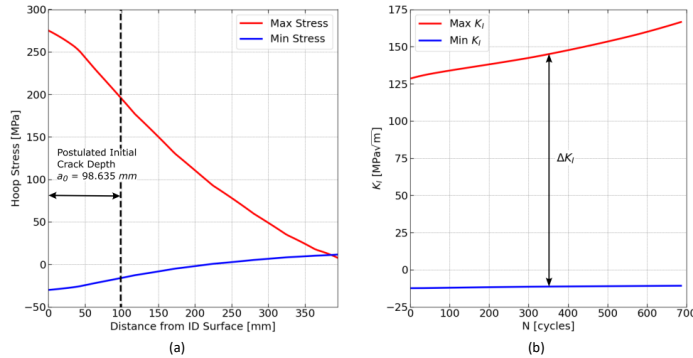


**FIGURE 5:** AN EXAMPLE OF (A) MAXIMUM AND MINIMUM HOOP STRESS PROFILES DURING TRANSIENT 2 (HEAT-UP AND COOL-DOWN) AND (B) THEIR CORRESPONDING STRESS INTENSITY FACTORS

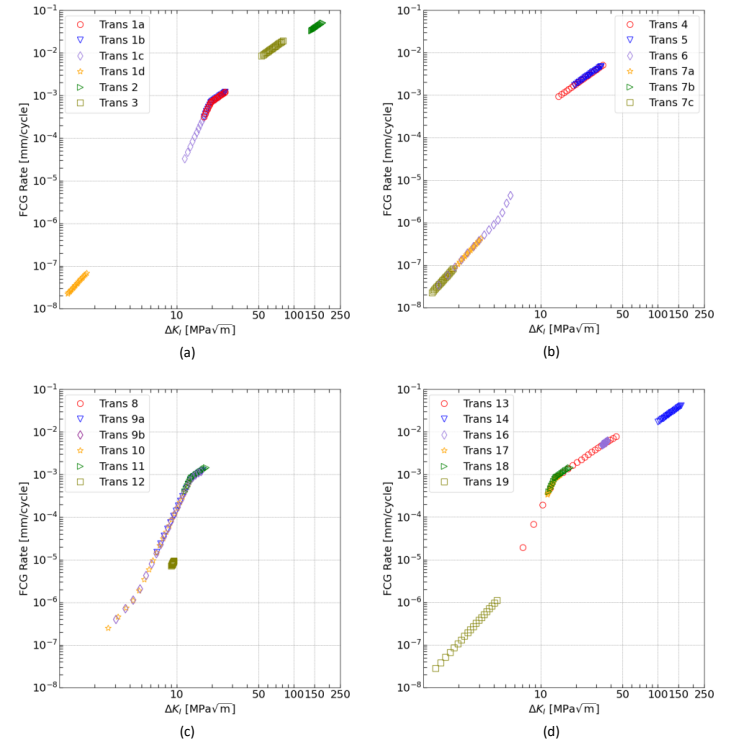
### 3.2 Fatigue Life Assessment

Fatigue life assessment was carried out at the critical location depicted in Figure 4, with an assumed initial semi-elliptical surface-breaking flaw of depth  $a_0 = 0.25t$  and half crack length  $c_0 = 3a_0$  as mentioned in Section 2.3. The SIFs resulting from axial stresses, which drive circumferential flaw growth, for all transients are below the critical crack arrest values ( $K_{Ia}$ ), defined in Equation (5b). Therefore, the SIF range originating from axial stress cycling is essentially negligible, and the circumferential flaw remains stable with no growth. Consequently, the fatigue life results are reported for axial flaw growth, which is driven by hoop stress cycling. It is important to note that Transient 15 in Table 1 pertains to secondary-side leakage tests, whereas the RPV is part of the primary circuit. As a result, Transient 15 is excluded from the analysis.

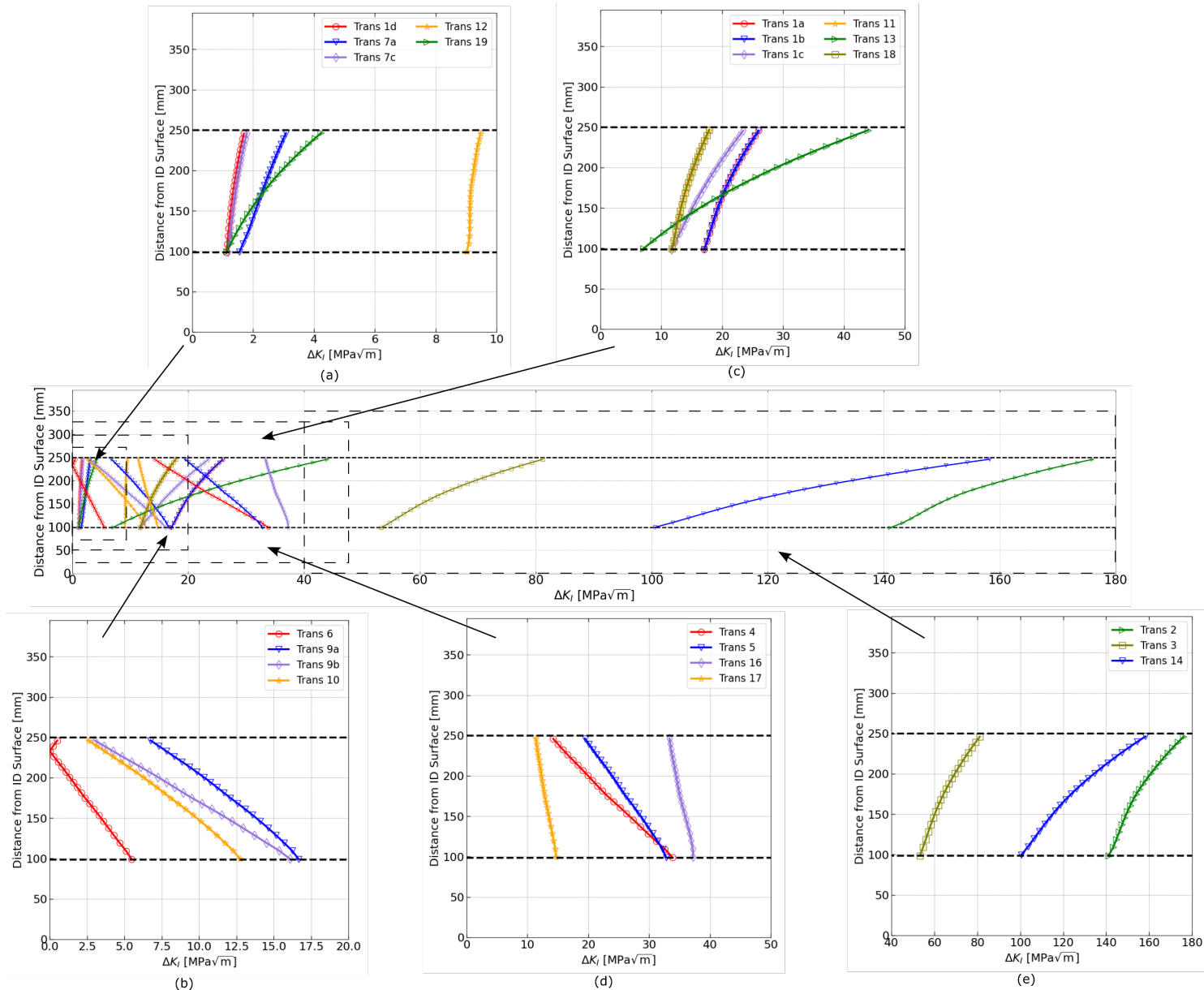
Figure 6 illustrates the FCG rate for axial flaw progression as a function of the SIF range. Transients 7b and 8 in Figure 6 (b) and (c), respectively, exhibit SIF ranges falling below the critical threshold  $\Delta K_{th}$ , defined in Equation (7b) applicable for high stress ratio  $R$ . As a result, no crack propagation is observed during these transients and accordingly no data points are shown for these transients. Transients 1d, 6, 7a, 7c, 12, 19 and parts of Transients 9b and 10 exhibit slow crack growth, below  $10^{-5}$  mm per cycle. Figure 6 (d) draws attention to Transient 19 (daily load follow operation), where a slow crack growth rate, mostly below  $10^{-6}$  mm per cycle, is evident.

Figure 7 compares the SIF range and FCG history attributed to all listed transients in Table 1, except for Transient 15. The cumulative impact of all transients influences the crack evolution. In Figure 7 (a), Transients 1d, 7a, 7c, 12, and 19 display low SIF ranges, thereby resulting in slow crack growth rates in accordance with the Paris Law given in Equation (6). Furthermore, the SIF ranges illustrate an increasing trend from the ID toward the OD. Even though Transient 19 (daily load-following operation) comprises 17,800 cycles for a 60-year design life, the magnitude of the SIF range remains small,

leading to a minimal impact on the overall fatigue life of the RPV. Conversely, in Figure 7 (b), Transients 6, 9a, 9b, and 10 feature slow FCG rates and reveal a decreasing SIF range as the crack advances through the vessel wall. Notably, Transient 6 demonstrates a reversal in the SIF range towards the OD due to the shift in the minimum stress profile overtaking the maximum stress profile, resulting in a larger SIF and a reversal of the SIF range. In Figure 7 (c), Transients 1a, 1b, 1c, 11, 13, and 18 exhibit moderate FCG rates and an increasing SIF range as the crack propagates through the vessel wall, whereas Figure 7 (d) illustrates that Transients 4, 5, 16, and 17 maintain moderate FCG rates but manifest a decreasing SIF range. Lastly, Figure 7 (e) highlights that Transients 2, 3, and 14 produce the largest SIF range, accompanied by an increasing SIF range, thereby resulting in the fastest FCG rates and the most influence on the overall fatigue life. Figure 8 shows the FCG history due to the combined effect of all the transients. It can be seen that the crack exhibits monotonic growth due to positive SIF ranges generated by these combined transients.



**FIGURE 6:** FATIGUE CRACK GROWTH RATES FOR ALL TRANSIENTS



**FIGURE 7: STRESS INTENSITY FACTOR RANGES AT THE DEEPEST POINT**

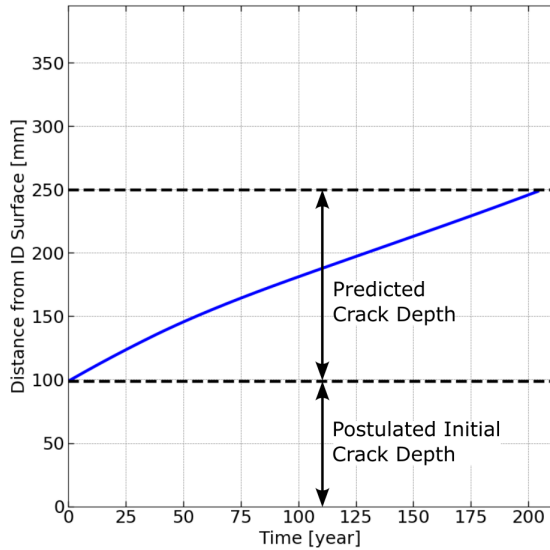


**FIGURE 8: TOTAL FATIGUE CRACK GROWTH HISTORY**

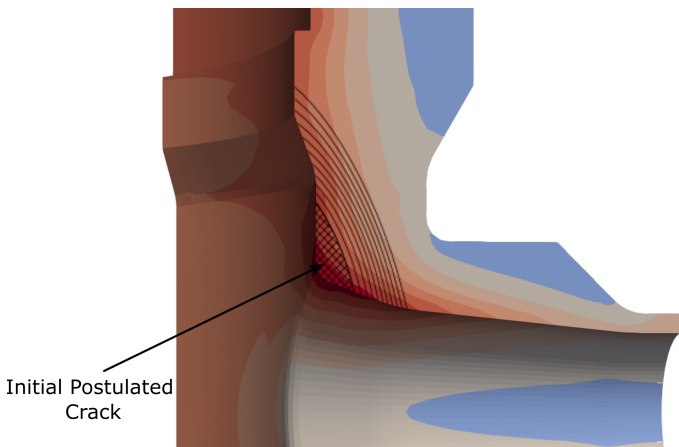


**FIGURE 9: CRACK GROWTH PREDICTION OF AN IDEALIZED SEMI-ELLIPTICAL SURFACE-BREAKING FLAW IN THE INLET NOZZLE**

It is important to note that even though the flaw is assumed to initiate at an angle at the corner of the inlet nozzle, the equations employed for SIF calculations from the ASME Section XI are for cylindrical geometry. This introduces a potential source of errors in both the SIF estimates and, consequently, the FCG history. Nevertheless, as illustrated in reference [20], SIF calculations for axis-aligned flaws are generally more conservative than SIF calculations for off-axis flaws. Explicit representation of the flaw within the model will be undertaken in future work to better account for the geometry and, consequently, refine SIF estimates and FCG predictions.

Figure 9 illustrates the crack growth prediction for the postulated idealized semielliptical surface-breaking flaw. Each contour in the figure represents a step in the propagation of the crack, starting from the initial assumed shape, indicated in a crosshatch pattern, and continuing until the final predicted shape.

These contours are spaced at 20 year intervals, providing a visual representation of the crack evolution over time.

#### 4. SUMMARY

In this study, a FE model of a light-water RPV was developed to investigate the fatigue life of the RPV under flexible load-following operating conditions. A coupled thermomechanical analysis was utilized to evaluate the stress response of the RPV. Subsequently, a critical location on the RPV was identified, and stress profiles were extracted along a critical path (i.e., the shortest path from the ID to the OD of the vessel). The SIFs for postulated idealized semi-elliptical flaw shapes were calculated following the ASME Boiler and Pressure Vessel Code, Section XI. The fatigue life assessment of the RPV was conducted using the linear elastic fracture mechanics approach.

The fitness-for-service analysis shows that the postulated circumferential flaw, driven by axial stress cycling, remains stable with no growth. As a result, the fatigue life is reported for the postulated axial flaw, driven by hoop stress cycling. The analysis of the fatigue life under varying loading conditions consisting of 19 transients (events) expected during a flexible load-following operation provides insights into transient stress experienced by the RVP:

- Transients 1d, 6, 7a, 7c, 9a, 9b, 10, 12, and 19 exhibit low FCG rates,
- Transients 1a, 1b, 1c, 4, 5, 11, 13, 16, 17, and 18 maintain moderate FCG rates,
- Transients 7b and 8 have no discernible impact on the fatigue life of the RPV,
- Transients 2 (heat-up and cool-down), 3 (unit loading and unloading at 5% per minute between 0% and 15% of full power), and 14 (primary-side leakage test) display high FCG rates, significantly impacting the fatigue life of the RPV,
- Transient 19 (daily load-following operation) has a low FCG rate, leading to minimal impact on the fatigue life.

Based on the fitness-of-service analysis conducted, it is evident that the analyzed RPV can be employed alongside intermittent energy sources in an integrated electric grid with no significant reduction in fatigue life. This conclusion stems from the finding that the thermo-mechanical cycling induced by the daily load-following operation transient (Transient 19), as part of flexible load-following operating conditions, has limited effect on the FCG rates.

#### ACKNOWLEDGEMENTS

This study is supported by the Australian Nuclear Science and Technology Organisation.

This manuscript was authored by Battelle Energy Alliance, LLC under contract no. DE-AC07-05ID14517 with the U.S. Department of Energy. The U.S. Government retains a nonexclusive, paid-up, irrevocable, worldwide license to publish or reproduce the published form of this manuscript, or allow others to do so, for U.S. Government purposes.

## REFERENCES

- [1] *Non-baseload Operation in Nuclear Power Plants: Load Following and Frequency Control Modes of Flexible Operation*. Vienna: INTERNATIONAL ATOMIC ENERGY AGENCY, 2018.
- [2] A. M. Foley, B. P. Ó Gallachóir, J. Hur, R. Baldick, and E. J. McKeogh, "A strategic review of electricity systems models," *Energy*, vol. 35, no. 12, pp. 4522-4530, 2010/12/01/2010, doi: <https://doi.org/10.1016/j.energy.2010.03.057>.
- [3] D. T. Ingersoll, C. Colbert, Z. Houghton, R. Snuggerud, J. W. Gaston, and M. Empey, *Can nuclear power and renewable energies be friends?* In: Proceedings of ICAPP 2015. Nice, France, 2015.
- [4] G. Ablay, "A modeling and control approach to advanced nuclear power plants with gas turbines," *Energy Conversion and Management*, vol. 76, pp. 899-909, 2013/12/01/2013, doi: <https://doi.org/10.1016/j.enconman.2013.08.048>.
- [5] C. Joint Research, E. Institute for, Transport, A. Eriksson, C. Bruynooghe, and G. Fulli, *Load-following operating mode at Nuclear Power Plants (NPPs) and incidence on Operation and Maintenance (O&M) costs – Compatibility with wind power variability*. Publications Office, 2010.
- [6] O. K. Chopra and W. J. Shack, "A review of the effects of coolant environments on the fatigue life of LWR structural materials," (in English), *J. Pressure Vessel Technol.*, vol. 131, no. ANL/NE/JA-60691; Journal ID: ISSN 0094-9930; JPVTAS; TRN: US1000745, p. Medium: X; Size: 021409, 2009, doi: 10.1115/1.3027496.
- [7] *Westinghouse Electric, 2011. Westinghouse AP1000 Design Control Document, Revision 19, June 2011. US-NRC Publication*.
- [8] Juergen Riegel, Werner Mayer, Yorik van Havre, and others (2001-2023). *FreeCAD (Version 0.21.1)*. [Software] Available from <http://www.freecadweb.org>.
- [9] *Coreform Cubit (Version 2022.11)* [Computer software]. Orem, UT: Coreform LLC. Retrieved from <http://coreform.com>.
- [10] "BlackBear Source Code Repository," <https://github.com/idaholab/blackbear>
- [11] A. D. Lindsay *et al.*, "2.0 - MOOSE: Enabling massively parallel multiphysics simulation," *SoftwareX*, vol. 20, p. 101202, 2022/12/01/ 2022, doi: <https://doi.org/10.1016/j.softx.2022.101202>.
- [12] O. Muránsky, M. C. Smith, P. J. Bendeich, and L. Edwards, "Validated numerical analysis of residual stresses in Safety Relief Valve (SRV) nozzle mock-ups," *Computational Materials Science*, vol. 50, no. 7, pp. 2203-2215, 2011/05/01/2011, doi: <https://doi.org/10.1016/j.commatsci.2011.02.031>.
- [13] J. P. Holman, *Heat Transfer*, 10th ed. McGraw-Hill Education, 2010.
- [14] W. M. Rohsenow, J. P. Hartnett, and Y. I. Cho, *Handbook of heat transfer*, 3rd ed. (McGraw-Hill handbooks). New York: McGraw-Hill (in English), 1998.
- [15] W. Wagner and H.-J. Kretzschmar, *International Steam Tables: Properties of Water and Steam based on the Industrial Formulation IAPWS-IF97*, 2nd ed. 2008.
- [16] ASME Boiler and Pressure Vessel Code, "Rules for Inservice Inspection of Nuclear Power Plant Components, Section XI, Division 1," ASME, New York, 2019.
- [17] H. F. Bueckner, "Novel principle for the computation of stress intensity factors," *Zeitschrift fur Angewandte Mathematik und Mechanik*, vol. 50, no. 9, pp. 529-546, 1970.
- [18] J. R. Rice, "Some remarks on elastic crack-tip stress fields," *International Journal of Solids and Structures*, vol. 8, no. 6, pp. 751-758, 1972/06/01/ 1972, doi: [https://doi.org/10.1016/0020-7683\(72\)90040-6](https://doi.org/10.1016/0020-7683(72)90040-6).
- [19] P. Paris and F. Erdogan, "A Critical Analysis of Crack Propagation Laws," *Journal of Basic Engineering*, vol. 85, no. 4, pp. 528-533, 1963, doi: 10.1115/1.3656900.
- [20] B. W. Spencer, W. M. Hoffman, and W. Jiang, "Weight function procedure for reduced order fracture analysis of arbitrary flaws in cylindrical pressure vessels," *International Journal of Pressure Vessels and Piping*, vol. 200, p. 104784, 2022/12/01/ 2022, doi: <https://doi.org/10.1016/j.ijpvp.2022.104784>.